

Synthesis of MnO₂ Nanoparticle Decorated Graphene-Based Porous Composite Electrodes for High-Performance Supercapacitors

D.N. Kang, J. Li, Y.H. Xu, W.X. Huang*

School of Materials Engineering, Shanghai University of Engineering Science, Shanghai 201620, China

*E-mail: jacob_lijun@163.com

Received: 6 March 2020 / *Accepted:* 7 April 2020 / *Published:* 10 June 2020

Transition metal oxides with nanostructures as electrode materials have become a popular topic for supercapacitors. A novel and simple approach was proposed to fabricate MnO₂ nanoparticles on reduced graphene oxide (RGO). RGO was firstly deposited on nickel foam using electrophoretic deposition accompanied by subsequent thermal reduction. Then, MnO₂ was deposited on RGO by electrodeposition with the applied potential of 0.6 V (vs. SCE) for 30 s. The morphology and structure of the deposits were analyzed in detail. Moreover, the electrochemical performance of MnO₂ nanoparticle decorated graphene-based porous composite electrodes was investigated comprehensively. The results indicated that a large number of MnO₂ nanoparticles with a diameter of approximately 5-50 nm were deposited on RGO that were independently separated by numerous fine gaps. The morphological characteristics endowed the electrode with a high specific area and short transfer path for electrons and active ions. The galvanostatic charge/discharge testing results indicated that the specific capacitance value of the electrode was calculated to be approximately 432 F·g⁻¹ at 1 A·g⁻¹. Approximately 55% of the initial specific capacitance was retained when the current density was sharply raised to 10 A·g⁻¹. MnO₂/RGO also demonstrated an outstanding cycling stability where 97.5% of the initial specific capacitance was reserved when undergoing 500 cycles.

Keywords: manganese dioxide; porous; supercapacitor; electrochemical performance

1. INTRODUCTION

Supercapacitors are considered a new energy storage device between a secondary battery and a traditional capacitor [1]. They show great application prospects in fields related to green chemical power supply owing to their good cycle life and high power density [2]. The material applied as the electrode is an essential factor for supercapacitors' electrochemical performance [3]. The most widely used electrode materials in supercapacitors are generally divided into transition metal oxides [4], conductive

polymers [5], and carbon materials [6]. Transition metal oxides with higher pseudocapacitance and fast redox kinetics have attracted extensive attention. Some (RuO_2 , NiO , Co_3O_4 , and MnO_2 [7-10] et al.) have been employed for supercapacitor electrode materials. Among various metal oxides, MnO_2 is regarded as a promising candidate for electrode materials owing to its high theoretical specific capacitance of approximately $1370 \text{ F}\cdot\text{g}^{-1}$, low production cost and good environmental friendliness [11]. Li et al. [12] synthesized MnO_2 powder by chemical precipitation. The electrodes were prepared by pressing the powder mixed with acetylene black (20%) and PTFE (polytetrafluoroethylene) binder (5%) under a 10 MPa pressure before mounting the powder on foamed nickel. The galvanostatic charge/discharge testing results demonstrated that the highest specific capacitance of the electrode reached $166 \text{ F}\cdot\text{g}^{-1}$ at $200 \text{ mA}\cdot\text{g}^{-1}$ in a 0.5 M Na_2SO_4 solution. Chodankar et al. [13] directly prepared MnO_2 thin films by means of the chemical bath deposition method on a flexible stainless steel substrate. A cyclic voltammetry (CV) test measured the highest specific capacitance of $145 \text{ F}\cdot\text{g}^{-1}$ at a scan rate of $5 \text{ mV}\cdot\text{s}^{-1}$ in a 0.5 M Na_2SO_4 solution. Similar studies had also indicated that the actual specific capacitance of a MnO_2 electrode was in the range of 130 to $185 \text{ F}\cdot\text{g}^{-1}$ [14-17], which was far below the theoretical value (only 15%). This very large contrast is attributed to its low conductivity, compact-packed structure with a low surface area, and lattice expansion/contraction during charging/discharging [18]. To solve the shortcomings mentioned above, various strategies have been proposed in recent years. One of them is building carbon-based materials (carbon nanotubes [19], carbon cloth [20], carbon nanofibers [21], and graphene [22] et al.) with MnO_2 . The produced synergistic effect results in a higher specific capacitance obtained in the composite electrodes. Carbon materials not only provide more valid transport channels for active ions and electrons owing to their large specific surface area but also enhance the charging/discharging rate resulting from their high conductivity. Moreover, these materials can significantly reduce volumetric changes during the charging/discharging cycles [23-24]. Zhao et al. [25] synthesized a carbon@ MnO_2 core shell hybrid nanosphere composite electrode by means of a hydrothermal method. A high specific capacitance of $252 \text{ F}\cdot\text{g}^{-1}$ was obtained at a scan rate of $2 \text{ mV}\cdot\text{s}^{-1}$ in a 1 M Na_2SO_4 solution. Moreover, the electrode also exhibited the outstanding cycling stability due to seventy-four percent of the initial specific capacitance retained after the electrode had experienced 2000 cycles. Su et al. [26] fabricated MnO_2 /carbon fiber paper (CFP) composite electrodes by a simple hydrothermal method. The specific capacitance was $251 \text{ F}\cdot\text{g}^{-1}$ at $1 \text{ A}\cdot\text{g}^{-1}$. A total of 98.9% of the initial specific capacitance was maintained for an electrode that underwent 3000 cycles. Other similar studies on MnO_2 /carbon composite materials had been carried out and confirmed that the specific capacitance and cycling stability were improved [27-30].

Graphene has been considered a promising supercapacitor electrode material owing to its large specific surface area, superior electrical conductivity, and outstanding chemical stability [31]. Recently, several successful studies on synthesizing MnO_2 /reduced graphene oxide (RGO) composites have been reported. Hao et al. [32] reported the rapid synthesis of MnO_2 /RGO by a polyaniline-assisted growth method. The prepared MnO_2 /RGO composite powder, acetylene black and polytetrafluoroethylene were mixed uniformly in the proportion of 16:3:1, and then the mixed slurry was coated onto nickel foam. The largest specific capacitance of $319 \text{ F}\cdot\text{g}^{-1}$ was acquired at $0.2 \text{ A}\cdot\text{g}^{-1}$. Mondal et al. [33] prepared MnO_2 /RGO hybrid nanosheets in ethylene glycol with vigorous stirring from a digital sonifier. The electrodes were produced by pressing slurries composed of MnO_2 /RGO, acetylene black (25%),

polyvinylidene difluoride (PVDF) (10%), and distilled N-methyl pyrrolidinone (NMP) onto titanium foil substrates. The galvanostatic charge/discharge testing results indicated that the largest specific capacitance of these electrodes was $320 \text{ F}\cdot\text{g}^{-1}$ at $0.5 \text{ A}\cdot\text{g}^{-1}$ in a $1 \text{ M Na}_2\text{SO}_4$ solution. The specific capacitance of these graphene and MnO_2 composite electrodes ranged from 305 to $389 \text{ F}\cdot\text{g}^{-1}$ [34-36]. However, MnO_2/RGO composites are usually in the form of powders and need to be mixed with some additional binders to fabricate the electrodes. These additions typically act as the “dead weight” of the electrodes and hinder the diffusion of ions in a way that significantly reduces the electrochemical performance of the electrodes [37]. Therefore, it is very urgent to find a new reproducible, additive-free method for preparing MnO_2/RGO supercapacitor electrodes.

In this paper, a three-step method was used to prepare a MnO_2/RGO composite electrode. First, graphene oxide films were fabricated on nickel foam by a simple and efficient method known as electrophoretic deposition (EPD). Thus, graphene oxide films were thermally reduced to graphene (called reduced graphene oxide, RGO) at a suitable temperature. Finally, composite electrodes with better performance could be obtained by depositing MnO_2 on RGO with the electrodeposition method. The resultant 3D composite electrode demonstrated outstanding electrochemical performance with respect to high specific capacitance, superior rate capability, and good cycling stability. The specific capacitance of the MnO_2/RGO electrode is superior to that of MnO_2 by the electrodeposition method and RGO by electrophoretic deposition.

2. EXPERIMENTAL METHOD

2.1 Preparation of the RGO electrode

The RGO electrode was prepared by electrophoretic deposition (EPD) accompanied by subsequent thermal reduction (TR). Prior to deposition, commercial nickel foam of 20 mm in width and 25 mm in height as the anode was ultrasonically treated for 30 min in a $1 \text{ mol}\cdot\text{L}^{-1}$ HCl solution to remove the NiO surface layer and subsequently cleaned by deionized water. Flaky graphite of 20 mm in width and 25 mm in height was selected as the cathode. GO powder (50 mg) was synthesized by a modified Hummers method. The powder was uniformly dispersed in 100 mL deionized water and ultrasonically processed for 2 h. Then, a suspension containing GO particles ($0.5 \text{ mg}\cdot\text{mL}^{-1}$) was formed, which was chosen as the electrolyte. A piece of nickel foam was placed between two pieces of graphite, among which a distance of 1 cm was maintained. EPD was carried out in a WYJ-300V2A steady flow power supply. A potential of 60 V was applied for 2 min. After deposition, the anode was air dried naturally. Finally, the deposited GO was turned into RGO under inert gas protection at $300 \text{ }^\circ\text{C}$ for 2 h. The weight of the RGO was measured by the difference between the weight of the pure nickel foam and that of the nickel foam covered with RGO.

2.2 Synthesis of the MnO_2/RGO electrode

A 0.5 M electrolyte for electrochemical deposition was obtained by dissolving 60.3 g manganese acetate into 500 mL deionized water. The electrochemical deposition was performed on a CHI 6082D

electrochemical workstation. To obtain a uniform MnO₂ coating on the RGO electrode, a constant voltage source of 0.6 V (vs. SCE) was used. The MnO₂/RGO electrode was held for 12 h at room temperature and weighed again to acquire the mass of MnO₂/RGO. The specific loading of MnO₂/RGO on nickel foam was about 0.16 mg·cm⁻².

2.3 Microstructural characterization

The phase constituents of the as-synthesized samples were analyzed by a PANalytical X' Pert Pro X-ray diffractometer. Their morphologies before and after depositing MnO₂ were observed by a HITACHI S-4800 field emission scanning electron microscope and a JEM-2100F transmission electron microscope. Raman spectra were collected to analyze the molecular structure using a HORIBA Raman spectrometer.

2.4 Electrochemical measurements

Cyclic voltammetry (CV) and galvanostatic charge/discharge tests were applied to evaluate the electrochemical performance on an electrochemical workstation. A 0.5 M Na₂SO₄ solution was selected as the electrolyte. A traditional three-electrode system was used, in which the working electrode and the counter electrode were the nickel foam coupled with RGO or MnO₂/RGO and the graphite sheet, and the reference electrode was the saturated calomel electrode (SCE). CV tests were carried out at five scan rates (0.005, 0.01, 0.05, 0.1 and 0.3 V·s⁻¹) in a potential window of 0.2 to 0.8 V (vs. SCE). Galvanostatic charge/discharge tests were performed at five current densities (1, 1.5, 3, 5 and 10 A·g⁻¹) in a potential range of -0.2 to 0.8 V.

3. RESULTS AND DISCUSSION

3.1 Microstructural characterization

Fig. 1 shows the morphological evolution of the deposited graphene oxide (GO) film before and after thermal reduction (300 °C). For the initial nickel foam, a reticulate structure can be clearly observed, in which a large number of branches are connected with each other and considerable pores are remained (Fig. 1(a)). The surface of the nickel foam is comparatively smooth in a low-magnification image (Fig. 1(a)). However, numerous equiaxed grains with diameters from 2 μm to 10 μm are identified in a high-magnification image (Fig. 1(b)). The surface of the nickel foam becomes comparatively rough and some corrugated patterns adhere to the surface when EPD is carried out at the applied potential of 60 V for 2 min (Fig. 1(c)). The grains on the surface of the nickel foam are almost not visible due to their surface being covered with many fold-like substances (Fig. 1(d)), which indicates that GO was successfully deposited on the nickel foam by EPD. Moreover, no cracks or peeling phenomena are observed, implying that the GO film tightly adheres to the surface of the nickel foam. After thermal reduction (300 °C) for 2 h, the fold-like patterns become more obvious (Fig. 1(e) and (f)), which is

attributed to the efficient removal of the oxygen-containing functional groups in the graphene oxide (Fig. 2). A high-quality reduced graphene oxide (RGO) electrode was successfully prepared. Finally, the MnO₂/RGO electrode was obtained by directly electrodepositing MnO₂ particles on the RGO surface with an applied potential of 0.6 V for 30 s. The whole preparation process of the composite electrode is illustrated in Fig. 3.

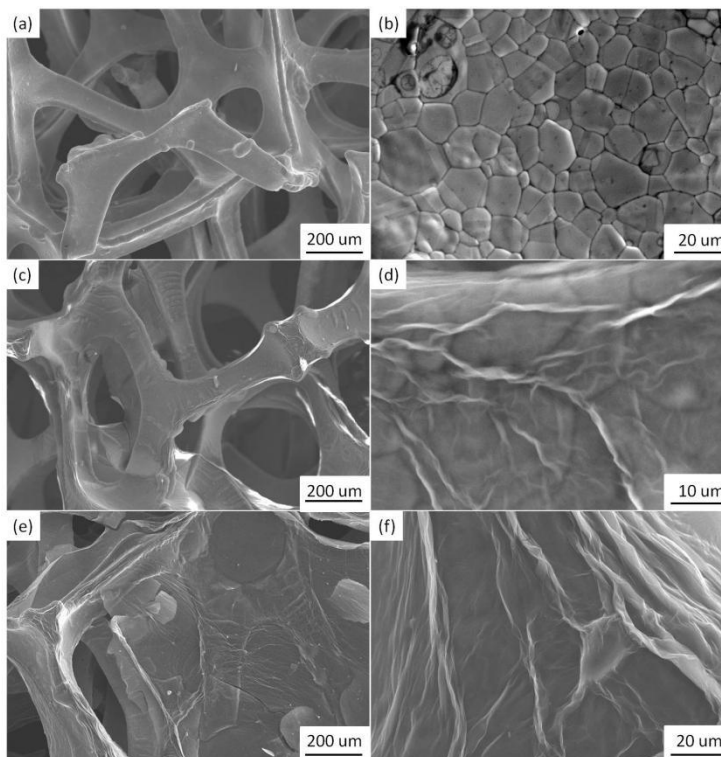


Figure 1. Morphological evolution of the nickel foam. (a), (b) initial nickel foam; (c), (d) after depositing GO; (e), (f) after thermal reduction of the deposited GO.

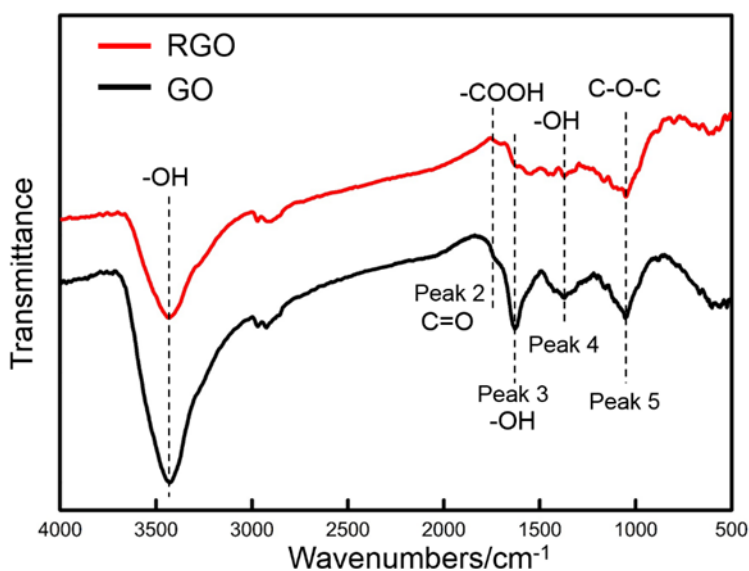


Figure 2 FTIR curves of GO and RGO.

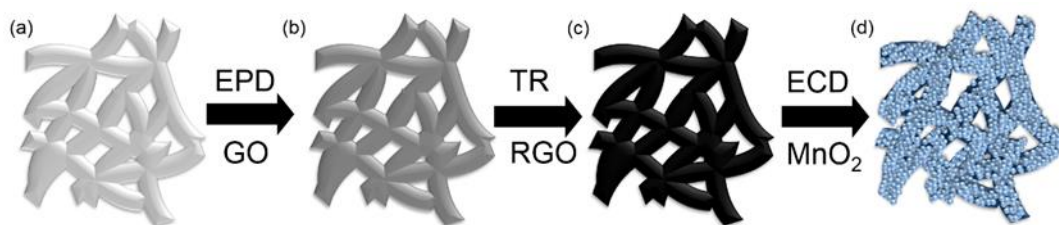


Figure 3. Schematic diagram for the preparation process of the MnO₂/RGO electrode.

Fig. 4 shows the XRD patterns of RGO and MnO₂/RGO. Three sharp peaks are located at $2\theta=44.6^\circ$, $2\theta=51.9^\circ$ and $2\theta=76.4^\circ$ that are in good agreement with those in JCPDS card No. 04-0850 for Ni. This indicates that nickel foam is very stable during the whole preparation of the composite electrode. A weak and broad (002) peak near 24° can be identified as a characteristic peak belonging to RGO [38]. After electrodeposition, two broader and weaker peaks are clearly observed at $2\theta=37^\circ$ (211) and $2\theta=65.5^\circ$ (002) that agree well with those in JCPDS card No. 44-0141 for α -MnO₂, suggesting that α -MnO₂ is successfully deposited on RGO.

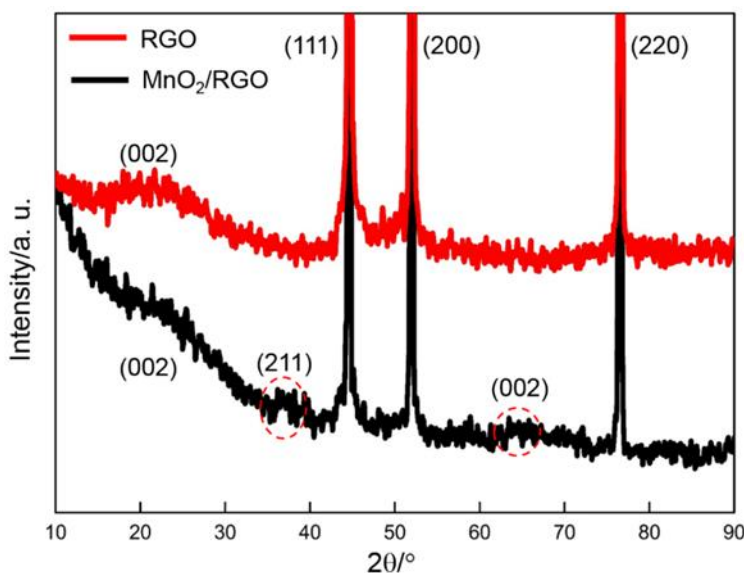


Figure 4. XRD patterns of RGO and MnO₂/RGO.

Fig. 5 shows the FE-SEM images of the two kinds of electrodes. The prepared RGO electrode exhibits many wrinkle-like patterns, which has been reported in many previous studies [39]. Moreover, the patterns are mainly distributed around the edge of the nickel branch. These wrinkle-like patterns can be attributed to edge effects. The planar zone of the nickel branch is parallel with the graphite sheet as a counter electrode. The electric-power lines are perpendicular to the planar zone and uniformly distributed within the zone. Therefore, wrinkle-like patterns are hardly observed due to the similar thickness of the deposited RGO in the planar zone. However, the electric field strength is higher around the branch edge than in the planar zone due to the edge effect. The electric field is also not uniformly distributed in different regions of the edge due to different regions being different distances from the counter electrode. As a result, GO particles are preferentially deposited at the edge of the electrode and

present different deposition rates in different regions. Steps may be formed in the regions with different deposition rates, which ultimately results in the production of wrinkle-like patterns. On the other hand, the effect of gravity is also an important factor in production patterns. The electrode is covered with a thin layer of colloid with fluid after deposition. When the electrode is moved away from the GO dispersion, the colloid flows slowly under the force of gravity, resulting in wrinkle-like patterns. Therefore, noticeable wrinkles are observed in Fig. 5(a). These morphological characteristics can endow the electrode with a high specific surface area. After electrodeposition of MnO_2 , the wrinkle-like pattern is inherited well (shown in Fig. 5 (b) and (c)). A high-magnification image ($\times 100,000$) clearly demonstrates that the RGO surface is completely covered with a large number of equiaxed MnO_2 nanoparticles with an average diameter of approximately 5-50 nm. The majority of particles are distributed independently; the remainder are connected with each other to form irregularly striped or flower-like coarse particles. The whole surface of the composite electrode presents a honeycombed morphology, which further enhances its specific surface area. Manganese acetate is oxidized to MnO_2 by a three-electrode system, and the reaction is as follows [40]:



As shown in Eq. 1, the Mn^{2+} ions in the solution diffuse to the surface of the anode and are adsorbed on it. The Mn^{2+} ions are oxidized to MnO_2 .

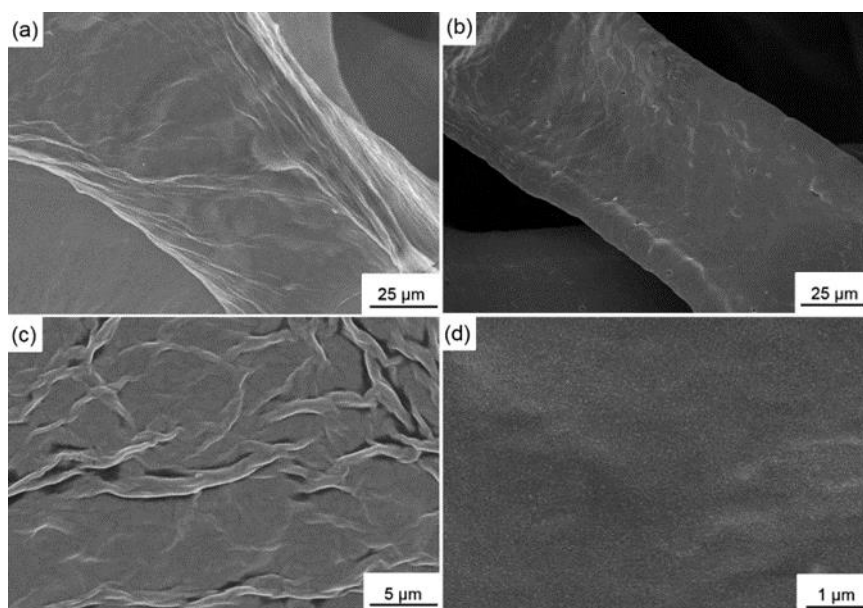


Figure 5. FE-SEM images of (a) RGO, (b), (c), and (d) MnO_2/RGO at different magnifications.

Fig. 6 shows the TEM results of MnO_2/RGO . A clear contrast in light can be observed in the bright field image (shown in Fig. 6), resulting in a dark irregular zone. The contrast formation is

attributed to the deposition of MnO₂ particles in the dark zones. A local area (marked with a circle in Fig. 6 (a)) is magnified to clearly show the morphology of the MnO₂ particles. As shown in Fig. 6(b) and (c), abundant equiaxed nanoparticles of 5–50 nm in diameter cluster together, and the result is exactly the same as that shown in SEM. Fig. 6(d) shows a high-resolution image of the equiaxed deposits.

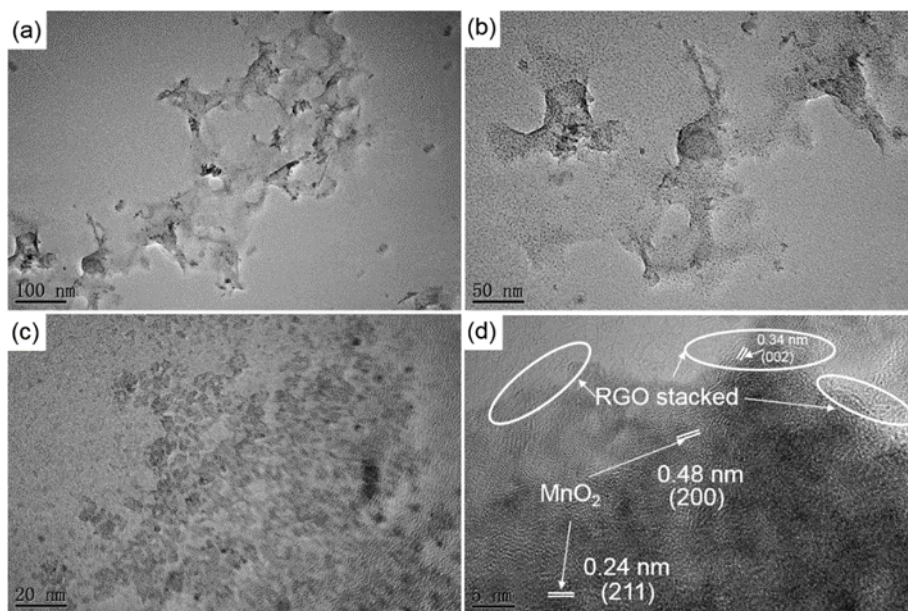


Figure 6. TEM images of (a), (b), (c), and (d) MnO₂/RGO at different magnifications.

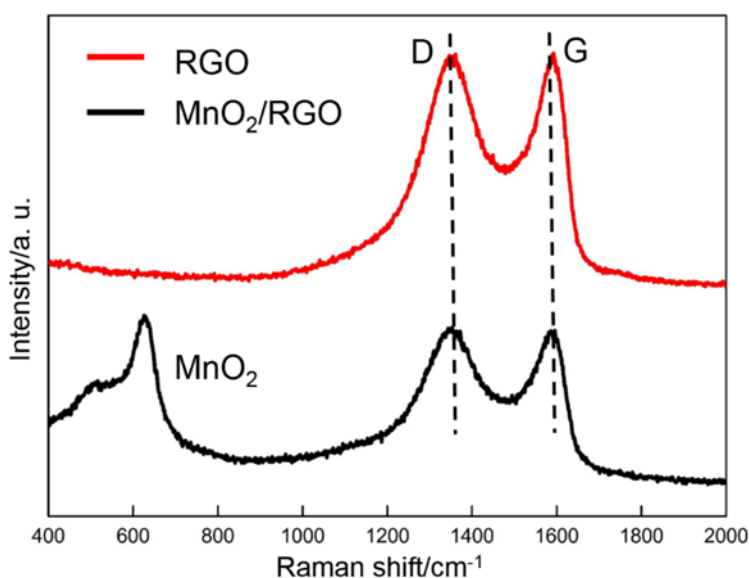


Figure 7. Raman spectra of RGO and MnO₂/RGO.

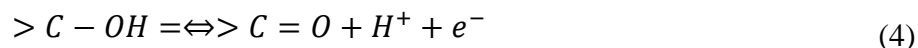
The dark zone can be confirmed to present good crystallization due to the large number of regularly arranged lattice fringes observed in the zone. Interplanar spacings of approximately 0.48 nm

and 0.24 nm were measured from the crystalline zones, which are consistent with the (200) and (211) planes of MnO₂ [41]. River-like patterns can be clearly observed around MnO₂ particles (as marked by white ellipses in Fig. 6(d)), which can be identified as a stacking zone consisting of multilayer RGO sheets [42]. One layer of RGO is deposited on the other, and a step remains that looks like a slip line observed in the plastically deformed metal or alloy. A large number of steps result in the formation of river-like patterns. The distance between the two steps can be calculated to be approximately 0.34 nm.

Raman spectroscopy is applied to analyze the evolution of the molecular structure of the substance adhering to the nickel foam before and after depositing MnO₂. Fig. 7 indicates that two clear and independent characteristic peaks appear before depositing MnO₂ on the RGO/NF electrode, corresponding to the D-band at approximately 1337 cm⁻¹ and the G-band at approximately 1595 cm⁻¹. The existence of the D-band is mainly attributed to edges or defects [43]. The G-band is associated with the E_{2g} phonon located at the Brillouin zone [44]. After depositing MnO₂, a new and strong peak appears at 627 cm⁻¹ in addition to the D-band and the G-band. This band originates from the Mn-O vibrations perpendicular to the MnO₆ octahedral double strands of MnO₂ [45]. These results further confirm that the composite consisting of RGO and MnO₂ was synthesized successfully.

3.2. Electrochemical properties

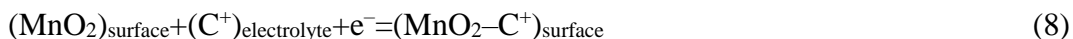
Cyclic voltammetry was used to evaluate the change in the specific capacitance of the MnO₂/RGO and RGO electrodes in a 0.5 M Na₂SO₄ electrolyte. Fig. 8 shows the CV profiles of MnO₂/RGO and RGO at a scan rate of 0.005 V·s⁻¹. It is obvious that the profile of the RGO electrode is approximately a rectangle, indicating that the double-layer capacitance is predominant. Some oxygen-containing functional groups (carboxyl, carbonyl, hydroxyl and epoxy groups) in RGO are retained after thermal reduction (shown in Fig. 2), which not only increases the wettability of the electrode surface but also provides some pseudocapacitance [46]. The pseudocapacitance mainly originates from the reversible redox reactions between the oxygen-containing functional groups, which can be described as follows:



When a large number of MnO₂ particles are deposited on the RGO surface, the CV profile of the electrode exhibits remarkable pseudocapacitance behavior due to the CV profile deviating from a perfect rectangle, which results from the charge-discharge mechanism of MnO₂. As a kind of pseudocapacitance electrode material, two possible mechanisms can be considered during the faradaic redox transition of MnO₂ over the potential range [47-48]. One mechanism is closely related to the hydrogen ions in the electrolyte, which can be intercalated into the electrode during the reduction and deintercalated from the electrode during the oxidation. The redox reaction is as follows:



The other proposed mechanism is the adsorption of cations from the electrolyte (C⁺) on the electrode surface layers [49]:



The CV profile is increased approximately 2 times in the integrated area due to the deposition of MnO₂, which is attributed to the pseudocapacitance offered by the deposited MnO₂. It can be concluded that deposited MnO₂ nanoparticles with a large specific surface area contribute to improving the specific capacitance of the electrode. The following equation can be applied to evaluate the specific capacitance of the electrode:

$$C_m = \frac{\int idv}{2 \times m \times \Delta V \times S}, \quad (9)$$

in which C_m denotes the specific capacitance (F·g⁻¹), ∫ idV signifies the integrated area enclosed by the CV curves, m represents the active substance mass (g), and ΔV and S are the potential range (V) and the scan rate (V·s⁻¹), respectively.

The specific capacitance of the RGO electrode is 139 F·g⁻¹ and the specific capacitance of the MnO₂/RGO composite electrode is 360 F·g⁻¹ under a scan rate of 5 mV·s⁻¹.

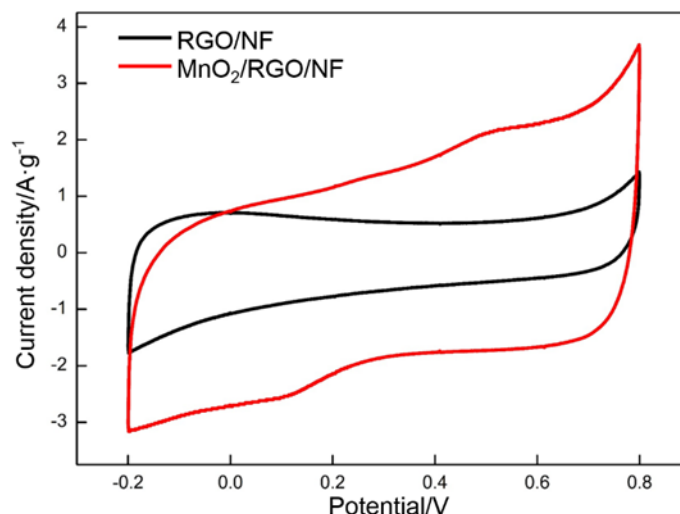


Figure 8. Comparison of CV curves of MnO₂/RGO and RGO electrodes at a scan rate of 0.005 V·s⁻¹.

The galvanostatic charge/discharge curves of RGO and MnO₂/RGO are shown in Fig. 9. The specific capacitance of RGO can be calculated as follows:

$$C_m = \frac{I \cdot \Delta t}{m \cdot \Delta v}, \quad (10)$$

where C_m represents the specific capacitance (F·g⁻¹), I denotes the discharge current (A), m is the active substance mass (g), and Δv and Δt are the potential range (V) and the discharge time (s), respectively.

The specific capacitance of the RGO/NF electrode is 151 F·g⁻¹. Reported studies [51-55] indicated that a pure graphene electrode exhibited a similar specific capacitance of approximately 140 F·g⁻¹ (as summarized in Table 1). The specific capacitance of the MnO₂/RGO composite electrode is 432 F·g⁻¹. The CV and galvanostatic charge–discharge testing results are highly consistent and indicate that the specific capacitance of the electrode consisting of MnO₂ is improved approximately 1.5 fold

compared to that without MnO₂. Moreover, the specific capacitance of the MnO₂/RGO electrode is higher than those of MnO₂ electrodes reported in some studies [12-17]. Some studies had indicated that MnO₂ exhibited an average specific capacitance of approximately 160 F·g⁻¹ (summarized in Table 2). The specific capacitance of the MnO₂/RGO electrode is enhanced to approximately 1.5 times that of the MnO₂ electrode. Similar results had been reported [32-36, 38]. As shown in Table 3, the average value of the specific capacitance of the MnO₂/RGO electrodes in some studies is approximately 340 F·g⁻¹, which is higher than that of the MnO₂ or RGO electrodes. However, the value is approximately 80% of that reported in our study. This difference may be attributed to the large specific surface area of the electrode, which allows sufficient contact between the electrolyte and electrode surface and offers a short diffusion path for active ions and electrons. The free binder in the preparation of the electrode is the other factor contributing to the increase in specific capacitance, which reduces the internal resistance and accelerates the prompt diffusion of active ions and electrons [50].

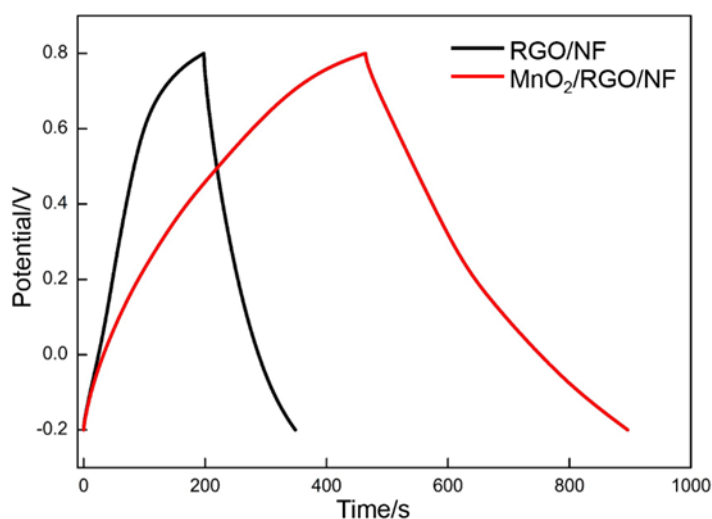


Figure 9. Galvanostatic charge/discharge curves of MnO₂/RGO and RGO electrodes at 1 A·g⁻¹.

Table 1. The specific capacitance values of RGO electrodes in the reported references.

Electrode	Specific capacitance (F·g ⁻¹)	Current density or scan rate	Reference s
RGO	164	10 mV·s ⁻¹	[51]
RGO	132	10 mV·s ⁻¹	[52]
RGO	141	1.04 A·g ⁻¹	[53]
RGO	117	100 mV·s ⁻¹	[54]
RGO	135	128 mA·g ⁻¹	[55]

Table 2. The specific capacitance values of pure MnO₂ electrodes in reported references.

Electrode	Specific capacitance (F·g ⁻¹)	Current density or scan rate	References
MnO ₂	166	200 A·g ⁻¹	[12]
MnO ₂	145	5 mV·s ⁻¹	[13]
MnO ₂	130	5 mV·s ⁻¹	[14]
MnO ₂	167	2.5 mA·g ⁻¹	[15]
MnO ₂	185	5 mA·cm ⁻²	[16]
MnO ₂	166	5 mV·s ⁻¹	[17]

Table 3. The specific capacitance values of MnO₂/RGO electrodes in reported references.

Electrode	Specific capacitance (F·g ⁻¹)	Current density or scan rate	References
MnO ₂ /RGO	319	0.2 A·g ⁻¹	[32]
MnO ₂ /RGO	320	0.5 A·g ⁻¹	[33]
MnO ₂ /RGO	305	5 mV·s ⁻¹	[34]
MnO ₂ /RGO	389	1 A·g ⁻¹	[35]
MnO ₂ /RGO	328	100 mV·s ⁻¹	[36]
MnO ₂ /RGO	392	1 A·g ⁻¹	[38]

As demonstrated in Fig. 6, MnO₂ nanoparticles can be deposited dispersedly by applying a suitable experimental parameter, and the connection phenomenon among the particles is hardly observed. The morphological characteristics endow the electrode with a high specific surface area. Previous studies had indicated that electrodes with high surface areas can efficiently improve electrochemical performance [17]. A large specific surface area can provide more electrochemically accessible sites for cation intercalation/deintercalation reactions due to the fuller contact between the electrode and the electrolyte. Moreover, fine nanoparticles can minimize the adverse effect of low-conductivity MnO₂ on the electrochemical performance. Therefore, MnO₂ nanoparticles with a honeycombed structure can provide a high contact area and short diffusion path for ions and electrons, which results in a remarkable enhancement in the charging/discharging rate and specific capacitance.

Fig. 10 indicates the CV profiles of MnO₂/RGO obtained at five scan rates. A profile similar to a rectangle is still acquired at a high scan rate of 0.3 V·s⁻¹, implying that MnO₂/RGO/NF demonstrates an outstanding capacitance performance. Using Eq. 9, the specific capacitance values of the composite electrodes were calculated as 136 F·g⁻¹ at 0.3 V·s⁻¹, 195 F·g⁻¹ at 0.1 V·s⁻¹, 232 F·g⁻¹ at 0.05 V·s⁻¹, 300 F·g⁻¹ at 0.01 V·s⁻¹, and 360 F·g⁻¹ at 0.005 V·s⁻¹. The specific capacitance exhibits a decreasing trend with

increasing the scan rate. With the change, however, the charging/discharging duration is correspondingly reduced. The charging/discharging duration is determined as follows: 7 s at $0.3 \text{ V}\cdot\text{s}^{-1}$, 20 s at $0.1 \text{ V}\cdot\text{s}^{-1}$, 40 s at $0.05 \text{ V}\cdot\text{s}^{-1}$, 200 s at $0.01 \text{ V}\cdot\text{s}^{-1}$, and 400 s at $0.005 \text{ V}\cdot\text{s}^{-1}$. The galvanostatic charge/discharge curves demonstrate an approximately symmetrical triangle when the current density is ranged from $1 \text{ A}\cdot\text{g}^{-1}$ to $10 \text{ A}\cdot\text{g}^{-1}$ (Fig. 11). The specific capacitances of the composite electrode were calculated as follows: $256 \text{ F}\cdot\text{g}^{-1}$ at $10 \text{ A}\cdot\text{g}^{-1}$, $296 \text{ F}\cdot\text{g}^{-1}$ at $5 \text{ A}\cdot\text{g}^{-1}$, $330 \text{ F}\cdot\text{g}^{-1}$ at $3 \text{ A}\cdot\text{g}^{-1}$, $385 \text{ F}\cdot\text{g}^{-1}$ at $1.5 \text{ A}\cdot\text{g}^{-1}$, and $432 \text{ F}\cdot\text{g}^{-1}$ at $1 \text{ A}\cdot\text{g}^{-1}$. The charging/discharging duration is 25.6 s, 59.2 s, 110 s, 257 s, and 432 s, respectively.

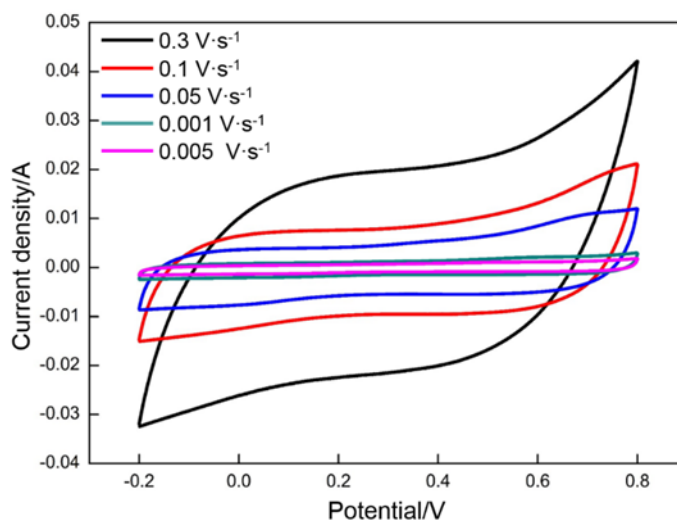


Figure 10. CV curves of MnO_2/RGO electrodes.

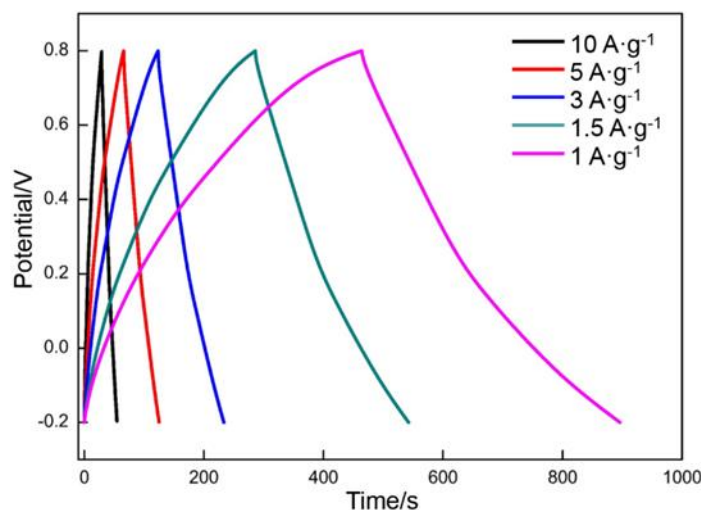


Figure 11. Galvanostatic charge/discharge curves of MnO_2/RGO electrodes.

The results obtained from the CV and galvanostatic charge–discharge tests all demonstrate that a high specific capacitance can be acquired at the cost of prolonging the charging/discharging time. This phenomenon is mainly in connection with the diffusion of ions in the electrolyte, which is directly

responsible for the EDLC and pseudocapacitance. The specific capacitance is reduced when the charging/discharging rate is higher than the diffusion rate of ions. In other words, the specific capacitance is increased as increasing the charging/discharging time because the internal resistance is decreased due to the faster insertion/extraction of the ions [26].

Fig. 12 indicates the change in specific capacitance with the scan rate and current density. Approximately 38% of the specific capacitance acquired at $0.005 \text{ V}\cdot\text{s}^{-1}$ can be maintained in the $\text{MnO}_2/\text{RGO}/\text{NF}$ electrode when the scan rate is sharply enhanced to $0.3 \text{ V}\cdot\text{s}^{-1}$. About 59% of the specific capacitance acquired at $1 \text{ A}\cdot\text{g}^{-1}$ is retained as the current density is sharply raised to $10 \text{ A}\cdot\text{g}^{-1}$. Therefore, it can be concluded that the $\text{MnO}_2/\text{RGO}/\text{NF}$ electrode demonstrates an excellent rate performance. It is clear that the specific capacitance exhibits different changes with reducing scan rate. When the scan rate is higher than $0.05 \text{ V}\cdot\text{s}^{-1}$, a good linear relationship between the two is maintained. However, the curve gradually deviates from the linear change when the scan rate is lower than $0.05 \text{ V}\cdot\text{s}^{-1}$, namely, the specific capacitance is enhanced more remarkably with increasing scan rate. The similar phenomenon was also observed for the galvanostatic charge/discharge tests. The critical value is determined to be $3 \text{ A}\cdot\text{g}^{-1}$. To obtain a comparatively high specific capacitance in a short period of time, $0.05 \text{ V}\cdot\text{s}^{-1}$ (CV) and $3 \text{ A}\cdot\text{g}^{-1}$ (galvanostatic charge/discharge) are optimum, in which approximately 70% of the initial value is maintained but only 10% of the charging/discharging time is applied.

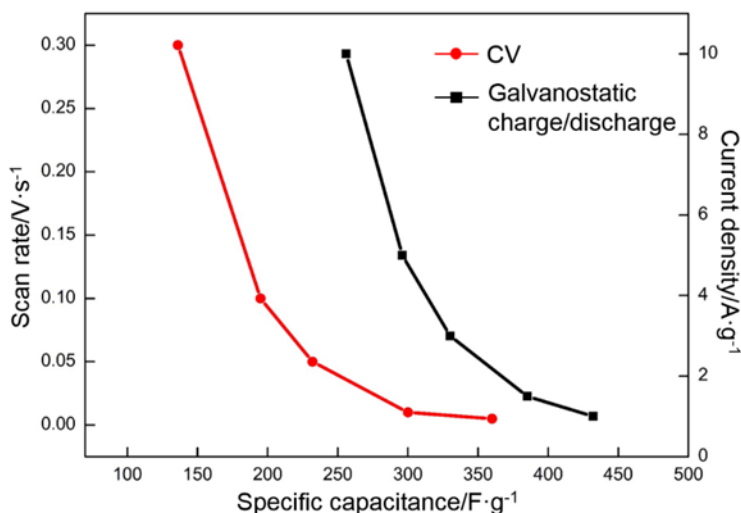


Figure 12. The effects of scan rate and current density on the specific capacitance of MnO_2/RGO electrodes.

The charging/discharging rate can be used as another important index characterizing the rate performance of a supercapacitor, referring to the obtained specific capacitance per unit time ($\text{F}\cdot\text{g}^{-1}\cdot\text{s}^{-1}$). As shown in Fig. 13, the index strongly depends on the scan rate (CV)/the current density (galvanostatic charge/discharge). The least squares method was used to process those data, and the results are described as follows:

For the CV tests $C=0.02776s+0.98238,$ (11)

For the galvanostatic charge/discharge tests $C=d,$ (12)

where C denotes the obtained specific capacitance per unit time ($F \cdot g^{-1} \cdot s^{-1}$) and s and d refer to the scan rate ($V \cdot s^{-1}$) and the current density ($A \cdot g^{-1}$), respectively.

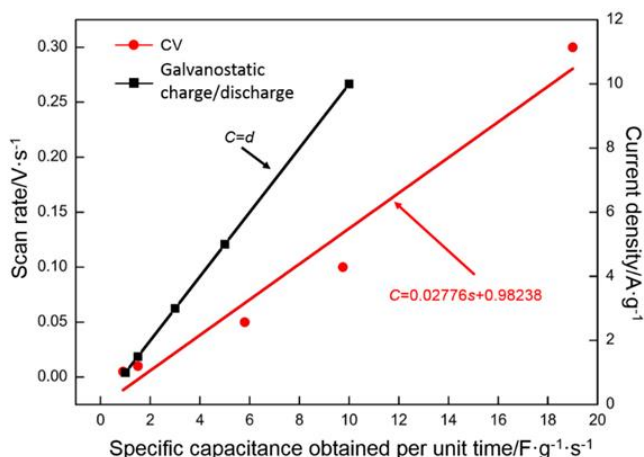


Figure 13. The effects of scan rate and current density on the obtained specific capacitance per unit time of $MnO_2/RGO/NF$.

The obtained specific capacitance per unit time linearly is increased with increasing the current density/scan rate. In other words, the charging/discharging efficiency can be improved by increasing the scan rate/current density. The specific capacitance obtained at $0.3 V \cdot s^{-1}$ is only half of that obtained at $0.005 V \cdot s^{-1}$ for the CV tests; however, the obtained specific capacitance per unit time is increased by approximately 20 times. The specific capacitance obtained at $10 A \cdot g^{-1}$ is only two thirds of that obtained at $1 A \cdot g^{-1}$ for the galvanostatic charge/discharge tests; however, the obtained specific capacitance per unit time is increased by 9 times. The high charging/discharging rate is attributed to the morphology of MnO_2/RGO . MnO_2 particles are deposited on RGO that are separated by numerous fine gaps.

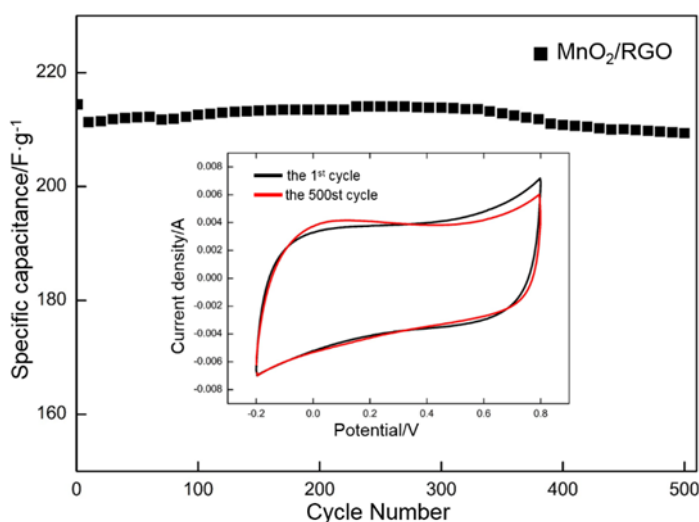


Figure 14. Cycling test for MnO_2/RGO at a scan rate of $0.05 V \cdot s^{-1}$ up to 500 cycles. The inset shows the CV curves with the first and 500th cycles.

The morphological characteristics endow MnO₂ with greater specific area, which can provide more active sites for the reverse redox reaction. Moreover, the synthesized MnO₂ particles are nanosized (with diameters of approximately 5–50 nm), which means that these particles can provide favorable and short conductive paths of ion diffusion and electron transfer in the three-dimensional directions. Therefore, the high specific area and short transfer path for ions and electrons result in the high charging/discharging rate of MnO₂/RGO [56]. These results further indicate that the MnO₂/RGO composite electrode possesses an outstanding rate performance.

4. CONCLUSIONS

(1) A high-quality MnO₂/RGO composite was successfully prepared on nickel foam by a simple path (GO was adhered to the surface of nickel foam by electrophoretic deposition, then was reduced to RGO at high temperatures, and MnO₂ nanoparticles were prepared by electrochemical deposition). Numerous MnO₂ particles with approximately 5–50 nm in diameter were uniformly distributed on RGO, among which numerous fine gaps were remained. The morphology efficiently improved the specific surface area of active substances and reduced the diffusion path of the electrons and active ions.

(2) The specific capacitance measured by cyclic voltammetry was 360 F·g⁻¹ under a scan rate of 5 mV·s⁻¹ in a 0.5 M Na₂SO₄ solution, and the specific capacitance measured by galvanostatic charge/discharge was 432 F·g⁻¹ at 1 A·g⁻¹ in a 0.5 M Na₂SO₄ solution.

(3) The specific capacitance was gradually reduced with increasing the charging/discharging rate. CV indicated that the value was reduced from 360 F·g⁻¹ (0.005 V·s⁻¹) to 136 F·g⁻¹ (0.3 V·s⁻¹). Galvanostatic charge/discharge showed that the value was reduced from 432 F·g⁻¹ (1 A·g⁻¹) to 256 F·g⁻¹ (10 A·g⁻¹). The obtained specific capacitance per unit time (F·g⁻¹·s⁻¹) had a linear relationship with the charging/discharging rate.

(4) The MnO₂/RGO deposited at 0.6 V demonstrated an outstanding cycling stability where approximately 97.5% of the initial specific capacitance was retained after undergoing 500 cycles.

ACKNOWLEDGMENTS

This work was funded by the National Natural Science Foundation of China (51471105), Shanghai University of Engineering Science Innovation Found (18KY0502) and the “Shu Guang” project of the Shanghai Municipal Education Commission (12SG44).

References

1. P. Yang, X. Xiao, Y. Li, Y. Ding, P. Qiang, X. Tan, W. Mai, Z. Lin, W. Wu, T. Li, H. Jin, P. Liu, J. Zhou, C. Wong, and Z. L. Wang, *ACS Nano*, 7 (2013) 2617.
2. Z. Xu, S. Sun, W. Cui, J. Lv, Y. Geng, H. Li, and J. Deng, *Electrochim. Acta*, 268 (2018) 340.
3. M. X. Guo, S. W. Bian, F. Shao, S. Liu, and Y. H. Peng, *Electrochim. Acta*, 209 (2016) 486.
4. X. Lia, and B. Wei, *Nano Energy*, 2 (2013) 159.
5. H. Yao, F. Zhang, G. Zhang, H. Luo, L. Liu, M. Shen, and Y. Yang, *Chem. Eng. J.*, 334 (2018) 2547.
6. Y. Li, B. Guan, A. Maclennan, Y. Hu, D. Li, J. Zhao, Y. Wang, and H. Zhang, *Electrochim. Acta*, 24

- (2017) 395.
7. K. S. Yang, Kim, C. H. Kim, and B. H. Kim, *Electrochim. Acta*, 174 (2015) 290.
 8. S. Zhu, Y. Dai, W. Huang, C. Zhang, Y. Zhao, L. Tan, and Z. Wang, *Mater. Lett.*, 161 (2015) 731.
 9. K. Qiu, Y. Lu, J. Cheng, H. Yan, X. Hou, D. Zhang, M. Lu, X. Liu, and Y. Luo, *Electrochim. Acta*, 157 (2015) 62.
 10. X. Tang, H. Li, H. Liu, Z. Yang, and Z. Wang, *J. Power Sources*, 196 (2011) 855.
 11. C. K. Lin, K. H. Chuang, C. Y. Lin, C. Y. Tsay, and C. Y. Chen, *Surf. Coat. Tech.*, 202 (2007) 1272.
 12. Y. Li, H. Q. Xie, and J. F. Wang, *Mater. Lett.*, 65 (2011) 403.
 13. N. R. Chodankar, D. P. Dubal, and G. S. Gund, *Curr. Appl. Phys.*, 165 (2015) 338.
 14. R. N. Reddy, and R. G. Reddy, *J. Power Sources*, 124 (2003) 330.
 15. M. W. Xu, L. B. Kong, W. J. Zhou, and H. L. Li, *J. Phys. Chem. C*, 111 (2007) 19141.
 16. B. Babakhani, and D. G. Ivey, *J. Power Sources*, 195 (2010) 2110.
 17. M. Toupin, T. Brousse, and D. Belanger, *Chem. Mater.*, 14 (2002) 3946.
 18. Z. Li, J. Wang, S. Liu, X. Liu, and S. Yang, *J. Power Sources*, 196 (2011) 8160.
 19. J. G. Wang, Y. Yang, Z. H. Huang, and F. Kang, *Electrochim. Acta*, 75 (2012) 213.
 20. P. A. Shinde, V. C. Lokhande, T. Ji, and C. D. Lokhande, *J. Colloid Interf. Sci.*, 498 (2017) 202.
 21. D. Zhou, H. Lin, F. Zhang, H. Niu, L. Cui, Q. Wang, and F. Qu, *Electrochim. Acta*, 161 (2015) 427.
 22. K. Ye, Z. Liu, C. Xu, N. Li, Y. Chen, and Y. Su, *Inorg. Chem. Commun.*, 30 (2013) 1.
 23. P. Ning, X. Duan, X. Ju, X. Lin, X. Tong, X. Pan, T. Wang, and Q. Li, *Electrochim. Acta*, 210 (2016) 754.
 24. X. Ma, P. Kolla, Y. Zhao, *J. Power Sources*, 325 (2016) 541.
 25. Y. Zhao, Y. Meng, and P. Jiang, *J. Power Sources*, 259 (2014) 219.
 26. X. Su, L. Yu, G. Cheng, H. Zhang, M. Sun, and X. Zhang, *Appl. Energ.*, 153 (2016) 94.
 27. T. Wanchaem, S. Rattanamai, P. D. Paisan, and K. W. Wongwiriyanpan, *Mater. Today*, 4 (2017) 6620.
 28. S. Liu, and D. Li, *Appl. Surf. Sci.*, 39 (2017) 33.
 29. L. Li, Z. A. Hu, N. An, Y. Y. Yang, Z. M. Li, and H. Y. Wu, *J. Phys. Chem. C*, 118 (2014) 22865.
 30. S. Zhu, W. Cen, L. Hao, J. Ma, L. Yu, H. Zheng, and Y. Zhang, *Mater. Lett.*, 13 (2014) 11.
 31. J. Li, X. Huang, and L. Cui, *Prog. Nat. Sci-Mater.*, 26 (2016) 212.
 32. J. Hao, Y. Zhong, Y. Liao, D. Shu, Z. Kang, X. Zou, C. He, and S. Guo, *Electrochim. Acta*, 167 (2015), 412.
 33. A. K. Mondal, B. Wang, D. Su, Y. Wang, S. Chen, X. Zhang, and G. Wang, *Mater. Chem. Phys.*, 143 (2014) 740.
 34. Y. Liu, X. Miao, J. Fang, X. Zhang, S. Chen, W. Li, W. Feng, Y. Chen, W. Wang, and Y. Zhang, *ACS Appl. Mater. Inter.*, 8 (2016) 5251.
 35. B. G. Choi, M. H. Yang, W. H. Hong, J. W. Choi, and Y. S. Huh, *ACS Nano*, 6 (2012) 4020.
 36. M. Kim, Y. Hwang, and J. Kim, *Chem Eng. J.*, 230 (2013) 482.
 37. T. S. Tran, K. M. Tripathi, B. N. Kim, I. K. You, B. J. Park, Y. H. Han, and T. Y. Kim, *Mater. Res. Bull.*, 96 (2017) 395.
 38. S. Ghasemi, R. Hosseinzadeh, M. Jafari, *Int. J. Hydrogen Energ.*, 40 (2015) 1037.
 39. F. Han, O. Qian, B. Chen, H. Tang, and M. Wang, *J. Alloy. Compd.*, 730 (2018) 386.
 40. Q. Huang, Y. Wang, X. Wang, J. Li, and G. Huang, *Chinese J. power sources*, 29 (2005) 470.
 41. C. L. Jin, N. Jin, M. X. Guo, P. Liu, J. N. Zhang, and S. W. Bian, *J. Colloid Interface Sci.*, 508 (2017) 426.
 42. L. Lu, T. M. Jeff, D. Hosson, and Y. Pei, *Mater. Des.* 144 (2018) 245.
 43. C. Casiraghi, A. Hartschuh, H. Qian, S. Piskanec, C. Georgi, A. Fasoli, K. S. Novoselov, D. M. Basko, and A. C. Ferrari, *Nano Lett.*, 9 (2009) 1433.
 44. S. J. An, Y. W. Zhu, and S. H. Lee, *Chem. Phys. Lett.*, 1 (2010) 1259.
 45. T. Gao, M. Glerup, F. Krumeich, R. Nesper, H. Fjellvag, and P. Norby, *Phys Chem C.*, 112 (2008) 13134.

46. J. Yan, Q. Wang, T. Wei, L. Jiang, M. Zhang, X. Jing, and Z. Fan, *ACS Nano*, 8 (2014) 4720.
47. M. Toupin, T. Brousse, and D. Belanger, *Chem. Mater.*, 16 (2004) 3184.
48. S. N. Devaraj, and Munichandraiah, *Phys. Chem. C*, 112 (2008) 4406.
49. F. Teng, S. Santhanagopalan, Y. Wang, and D. Desheng, *J. Alloy. Compd.*, 499 (2010) 259.
50. L. Zhang, T. Li, X. Ji, Z. Zhang, W. Yang, J. Gao, H. Li, C. Xiong, and A. Dang, *Electrochim. Acta*, 252 (2017) 306.
51. Y. Chen, X. Zhang, P. Yu, and Y. Ma, *J. Power Sources*, 195 (2010) 3031.
52. X. Liu, X. Qi, Z. Zhang, L. Ren, G. Hao, Y. Liu, Y. Wang, K. Huang, X. Wei, J. Li, Z. Huang, and J. Zhong, *RSC Adv.*, 4 (2014) 13673.
53. D. F. Yang, and B. Christina, *J. Power Sources*, 337 (2017) 73.
54. S. R. C. Vivekchand, C. S. Rout, and K. S. Subrahmanyam, *Chem. Sci.*, 120 (2008) 9.
55. M. D. Stoller, S. Park, Y. Zhu, J. An, and R. S. Ruoff, *Nano Lett.*, 8 (2008) 3498.
56. B. S. Singu, and K. R. Yoon, *Electrochim. Acta*, 231 (2017) 749.

© 2020 The Authors. Published by ESG (www.electrochemsci.org). This article is an open access article distributed under the terms and conditions of the Creative Commons Attribution license (<http://creativecommons.org/licenses/by/4.0/>).